The Meteoritical Society

Meteoritics & Planetary Science 49, Nr 12, 2219–2240 (2014)
doi: 10.1111/maps.12391

EH3 matrix mineralogy with major and trace element composition compared to chondrules

S. W. LEHNER[1*], W. F. McDONOUGH[2], and P. NÉMETH[3]

[1]School of Earth and Space Exploration, Arizona State University, Tempe, Arizona 85287, USA
[2]Department of Geology, University of Maryland, College Park, Maryland 20742, USA
[3]Institute of Materials and Environmental Chemistry, Research Center for Natural Sciences, Hungarian Academy of Sciences, Magyar Tudósok Körútja 2, H-1117 Budapest, Hungary
[*]Corresponding author. E-mail: slehner@asu.edu

(Received 22 October 2013; revision accepted 13 October 2014)

Abstract–We investigated the matrix mineralogy in primitive EH3 chondrites Sahara 97072, ALH 84170, and LAR 06252 with transmission electron microscopy; measured the trace and major element compositions of Sahara 97072 matrix and ferromagnesian chondrules with laser-ablation, inductively coupled, plasma mass spectrometry (LA-ICPMS); and analyzed the bulk composition of Sahara 97072 with LA-ICPMS, solution ICPMS, and inductively coupled plasma atomic emission spectroscopy. The fine-grained matrix of EH3 chondrites is unlike that in other chondrite groups, consisting primarily of enstatite, cristobalite, troilite, and kamacite with a notable absence of olivine. Matrix and pyroxene-rich chondrule compositions differ from one another and are distinct from the bulk meteorite. Refractory lithophile elements are enriched by a factor of 1.5–3 in chondrules relative to matrix, whereas the matrix is enriched in moderately volatile elements. The compositional relation between the chondrules and matrix is reminiscent of the difference between EH3 pyroxene-rich chondrules and EH3 Si-rich, highly sulfidized chondrules. Similar refractory element ratios between the matrix and the pyroxene-rich chondrules suggest the fine-grained material primarily consists of the shattered, sulfidized remains of the formerly pyroxene-rich chondrules with the minor addition of metal clasts. The matrix, chondrule, and metal-sulfide nodule compositions are probably complementary, suggesting all the components of the EH3 chondrites came from the same nebular reservoir.

INTRODUCTION

The origin and nature of chondrite matrix, material that is amorphous or with grains <5 μm in diameter, are debated (Scott et al. 1988). Suggestions include that it consists mainly of chondrule fragments (Alexander et al. 1989; Brearley 1996), CI-like material with an origin distinct from chondrules (Alexander 2005), reprocessed material from the parent molecular cloud of the solar system (Buseck and Hua 1993; Zolensky et al. 1993; Huss et al. 2005), and products of nebular condensation (Larimer and Anders 1967).

The enstatite chondrites (EC) were estimated to contain between 2 and 15 vol% matrix (Scott and Krot 2005; Rubin et al. 2009), material that has not been widely studied. EC are thought to have accreted in the inner solar system (Shukolyukov and Lugmair 2004). They are linked to Earth by nearly identical isotopic compositions of several major and minor elements (Javoy et al. 2010; Jacobsen et al. 2013; Kaminski and Javoy 2013), and they have been proposed as potential source material for Earth and the Moon (Clayton et al. 1984; Javoy 1995; Javoy et al. 2010). Therefore, like the EC chondrules, the matrix in highly unequilibrated EH3 chondrites potentially provides insight into events and materials from the early inner solar system.

Preliminary work showed that the EH matrix consists primarily of enstatite, cristobalite, troilite, and kamacite (Lehner and Buseck 2010; Lehner et al. 2012b). The abundant cristobalite suggests a possible link with sulfidized chondrules, which are a subset of EH3 chondrules in which forsterite and enstatite were

replaced by niningerite, troilite, and abundant cristobalite (Lehner et al. 2013b). An open question is whether there is a genetic relation between chondrules and matrix in EH chondrites.

To resolve that question, we used TEM to investigate the matrix in primitive EH3 chondrites Sahara 97072, ALH 84170, and LAR 06252 and measured the trace and major element compositions of matrix, chondrules, and bulk Sahara 97072. The goals were to describe EC matrix, to gain insight into the processes it experienced, and to determine whether and how it is related to the chondrules.

PRIOR WORK

A few papers mention EC matrix (Keil [1968]—EH4 Indarch; Kimura [1988]—EH3 Yamato-691; Leitch and Smith [1982]—EH3 Kota-Kota, EH4s Adhi-Kot, and Abee), and several papers report presolar grains in EH3 matrix including in Sahara 97072 (Huss and Lewis 1995; Ebata et al. 2006, 2008). The first study devoted to EC matrix (Rubin et al. 2009) described it as filling depressions in the chondrule surfaces for EH3s Yamato-691 and ALH 81189. They reported limited chemical variability among different matrix areas, that chondrules and matrix have the same O isotopic compositions, and suggested the low abundance of EH matrix points to accretion in a turbulent region of the nebula. Quirico et al. (2011), in a study of the structural order of matrix organic matter in a group of EH3 and EL3 chondrites, determined Sahara 97096, paired with Sahara 97072, to be among the least metamorphosed followed closely by ALH 84170. They described EH3 organic matter as having a polyaromatic structure similar to that found in CV, CO, and unequilibrated ordinary chondrites. Piani et al. (2012) described the insoluble organic matter in the matrix of EH3 Sahara 97096.

We have been studying EH3 matrix using transmission electron microscopy (TEM) and reported both amorphous and fine-grained material that consists of approximately 45 vol% enstatite, up to 30 vol% cristobalite, 15–20 vol% kamacite and troilite, with minor niningerite, oldhamite, and C-rich spherules. Much of the amorphous material is rich in SiO_2, contains Al, Na, Ca, or Fe, and encloses submicron clasts of typical EH chondrite minerals as well as the C-rich spherules (Lehner and Buseck 2010; Lehner et al. 2012b).

METHODS

We studied five thin sections of Sahara 97072, one thin section of ALH 84170, and two thin sections of LAR 06252. ALH 84170 and LAR 06252 were on loan from NASA Johnson Space Center. All are EH3s. We used petrographic microscopy and scanning electron microscopy (SEM) to identify locations of fine-grained material. Areas of interest were mapped for common elements using a field-emission source FEI XL30 scanning electron microscope equipped with energy dispersive spectroscopy. Mapped elements include Fe, S, P, Ni, Co, Mg, Si, O, C, Mn, Al, Cu, Cr, Ca, K, Na, N, and Zn.

A dual source SEM equipped with a Ga focused ion beam (FIB) was used to extract 10 to 20 μm slices from the petrographic thin sections of all three meteorites for study with transmission electron microscopy (TEM). Additional material from Sahara 97072 was randomly sliced, mounted on 3 mm Cu grids, and ion-milled to electron transparency for study with TEM and SEM.

High resolution transmission electron microscopy (HRTEM), scanning transmission electron microscopy (STEM), selected area electron diffraction (SAED), electron energy-loss spectroscopy (EELS), and energy dispersive spectroscopy (EDS) were performed using standard transmission electron microscopes including a Phillips CM 200, JEOL 2010F, JEOL 2000, and a JEOL 4000. EDS data were quantified using the Cliff–Lorimer thin-film approximation with theoretical k-factors. However, due to the extremely small grains and the inherent thickness of the TEM sections, most analyses consist of mixtures of more than one mineral or phase.

Laser-Ablation Inductively Coupled Plasma Mass Spectrometry

Selected areas of matrix and intact, nonsulfidized silicate chondrules were analyzed with laser-ablation, inductively coupled, plasma mass spectrometry (LA-ICPMS) using a New Wave Research UP213 laser-ablation unit. Also, four LA-ICPMS line scans were performed to approximate bulk composition, and spot analyses were obtained for troilite, oldhamite, niningerite, djerfisherite, kamacite, and schreibersite.

All areas were preablated to remove residual contamination. The beam was flashed at 5 Hz for 20 s with the shutter closed for background signal and then with the shutter open for approximately 40 s on the sample. The spot size ranged from 30 to 100 μm in diameter, and the laser energy ranged from 1.38 to 2.42 J cm^{-2}.

The ablated material was analyzed for 40 elements (Table A1) with a magnetic-sector, single-collector Thermo-Finnegan Element 2 ICPMS. The mass spectrometer was operated in a dynamic

peak-hopping mode, with mass/charge positioning achieved by a combination of magnetic current shifts and voltage offsets of the electrostatic analyzer (Hamester et al. 1999). The laser-ablation system was operated in aperture-imaging mode using a monochromatic 213 nm beam, which was generated from a frequency-quintupled, solid-state Nd-YAG source. This beam was focused onto a sample in a 3 cm^3 ablation cell, which was continuously flushed to the plasma source of the mass spectrometer with approximately 1.1 L min^{-1} He gas. Each analysis sequence consisted of two or three runs of standard reference materials before and after data acquisition of six to twelve spots.

All data were processed using LAMTRACE software (Achterbergh et al. 2001), which determines element concentrations based on ratios of background-subtracted count rates for samples and standards, known concentrations in the standards, and an internal standard for the unknowns. The detection limits for the LA-ICPMS measurements were set at the average background count rate plus three times the standard deviation of the background.

Standards for LA-ICPMS

National Bureau of Standards glass 610 was used as the external standard. The results for selected siderophile elements were checked against iron meteorites Filomena and Hoba (Walker et al. 2008). Internal standard values used to quantify the LA-ICPMS data were obtained using a JEOL JXA-8600 electron microprobe (EMP) with wavelength dispersive spectroscopy. Matrix and chondrules were measured adjacent to the laser pits after lightly polishing the thin sections to remove ablation debris. The EMP was calibrated with a 15 μm defocused beam using a 15 nA current, 15 kV accelerating voltage, and mineral standards. Analyses were made for O, Si, Mg, Ca, S, Fe, Na, Al, K, and Mn. For O analysis, we used Al_2O_3 as a standard and the layered dispersion element (LDE) spectrometer was run with the slits wide open to maximize the X-ray count; 15 μm spots were measured around individual laser pits to determine heterogeneity on the scale of the pits (approximately 40 μm).

A known value for an internal standard element must be input into the LAMTRACE software (Achterbergh et al. 2001) to calculate the concentration of all other elements. To obtain the internal standard values, we looked for elements with consistent concentrations around the laser pits measured by EMP. Except for O and Si, the major element concentrations varied substantially around both the matrix laser pits and chondrule laser pits with relative error ranging from 25 to 212%. The O/Si ratio (0.6) was quite consistent for the matrix analyses (7% relative error) and chondrule analyses (8% relative error). Therefore, for a given LA-ICPMS spot, we assumed the O/Si ratio was 0.6. The LA-ICPMS data were quantified by adjusting the input O and Si values iteratively while maintaining the EMP ratio of 0.6 until the total of all elements equaled approximately 1,000,000 ppm, or 1. The only major elements not analyzed with LA-ICPMS were Na and K, so we used their mean values from EMP analyses to achieve the total.

Higher Fe and S and lower Mg and Si concentrations were obtained for LA-ICPMS measurements than with the EMP, presumably because the larger spot size of the former included sulfide and metal fragments. However, the ratios between the major elements were similar for both methods. All LA-ICPMS and EMP values for the major elements in the chondrules and matrix display a statistical normal distribution. We therefore conclude that the means of the data are representative and useful for comparison of the data sets.

Bulk Analysis

Bulk analyses were performed by ALS CHEMEX (http://www.alsglobal.com/) on a 1.5 g sample that was pulverized in an agate mill. Four approximately 0.06 g aliquots were fused with $Li_2B_4O_7$ and dissolved in HNO_3 for major element analysis (method ME-ICP06) using inductively coupled plasma atomic emission spectroscopy (ICP-AES), and for analysis of 38 trace elements (method ME-MS81) using ICPMS (Table A1). A 0.4 g aliquot was analyzed for total C and S by combustion in a Leco induction furnace. CO_2 and SO_2 were measured with an infrared detector. The remaining material was dissolved using a four-acid digestion for analysis of 48 elements (method Me-MS61) using ICPMS (Table A1).

Additional bulk compositions were obtained by quantifying the four 100 μm wide and approximately 1 cm long LA-ICPMS line scans for 40 elements (Table A1). The results for the dissolution analyses and the LA-ICPMS line scans agree to within 25% except for Ca, Mn, and S, which are higher in the line scans, presumably from preferential sampling of oldhamite and niningerite. The data from all the methods were compiled, resulting in values for 63 elements. Those elements analyzed using several different methods, e.g., Mg, were measured multiple times, whereas certain elements, e.g., S, had only one measurement.

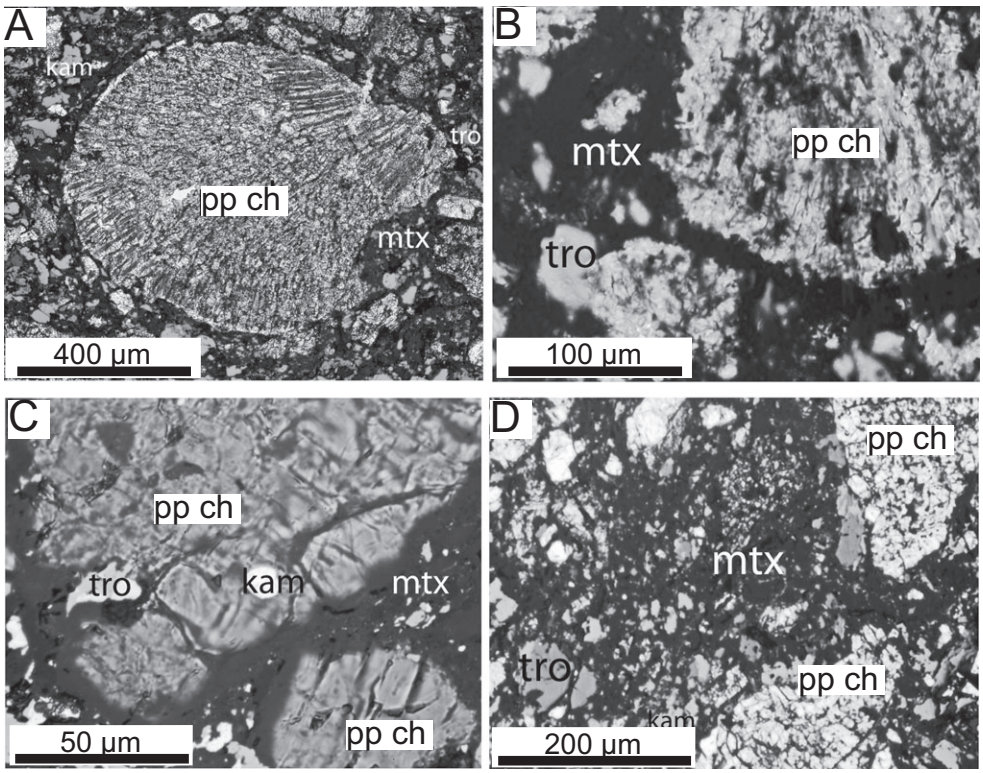

Fig. 1. Combined transmitted and reflected light images of chondrules and large clasts showing matrix with and without visible grains (dark material). A) Porphyritic pyroxene chondrule from LAR 06252 surrounded by matrix filled with silicate, kamacite, and troilite clasts. B) Typical chondrule and chondrule fragment from ALH 84170 separated by matrix enclosing troilite and enstatite. C) Typical chondrule and chondrule fragment from Sahara 97072 separated by matrix enclosing kamacite, troilite, and fine-grained silicates. D) Area from Sahara 97072 showing matrix hosting abundant clasts of sulfides, kamacite, and pyroxene. pp ch = porphyritic pyroxene chondrule, mtx = matrix, tro = troilite, en = enstatite, kam = kamacite.

Modal Proportions

The modal proportions of matrix from Sahara 97072, ALH 84170, and LAR 06252 were estimated by pixel counting photographs of petrographic thin sections taken with combined reflected and transmitted light at a magnification of 20x (Fig. 1). The contrast threshold was set using Image J software to render matrix black, with other material white. For all meteorites the black pixels in multiple images (82 for Sahara 97072, 12 for ALH 84170, and 6 for LAR 06252) were analyzed several times each and the results averaged to obtain an estimate of the percentage of matrix. Area was assumed to be a proxy for volume.

For Sahara 97072, estimates for the proportions of chondrules, silicate clasts, metal-sulfide nodules, and opaque clasts in the bulk meteorite are based on the modal analysis of Sahara 97096, which is paired with Sahara 97072 (Weisberg and Prinz 1998), average EH values (Zhang et al. 1995), and observations of five approximately 1.5 × 3 cm petrographic thin sections of Sahara 97072 (Table 1). The component proportions of ALH 84170 and LAR 06252 appear to be similar to Sahara 97072.

RESULTS

EH3 Petrography

Petrographically Sahara 97072, ALH 84170, and LAR 06252 are similar. Their chondrules and chondrule fragments have sharp boundaries (Fig. 1A), are typically porphyritic pyroxene with minor olivine, and most of them are between 100 and 500 μm in diameter with a few much larger, up to 3 mm. All three meteorites contain cryptocrystalline chondrules, which are most abundant in ALH 84170. They are all breccias containing abundant chondrule fragments, as well as silicate, metal, and sulfide clasts (Lehner and Buseck 2009).

Of the three meteorites, ALH 84170 is the most weathered (grade B) with brown limonitic staining throughout the section. LAR 06252 and SAH 97072 have modest weathering restricted to certain areas.

Table 1. Modal analysis of Sahara 97072, which was based on the analysis of Sahara 97096, which is paired with Sahara 97072 (Weisberg and Prinz 1998), average EH values (Zhang et al. 1995), and observations of five approximately 1.5 × 3 cm petrographic thin sections, which included pixel counting of 82 photographs of petrographic thin sections taken with combined reflected and transmitted light at a magnification of 20x (see the Methods section).

Components (area %)	% of meteorite	Silicates %	Metal %	Sulfides %	Total
Chond. and sil. clasts	41	95.1	2.4	2.4	100
MSN and opq. clasts	37	13.5	62.2	24.3	100
Matrix	22	77.3	13.6	9.1	100
SAH bulk	100	62.0	26.1	12.0	100

Sahara 97072 contains shock features in the form of opaque veins which are composed of kamacite and troilite in simplectic intergrowth indicating a quenched eutectic melt. It was assigned shock stage S3-4 (Quirico et al. 2011). However, these veins are localized and most areas are completely free of them.

In addition to silicate chondrules, these meteorites contain abundant metal-sulfide nodules (MSN) that are typical of EH3s (Figs. 2A–C) (Ikeda 1989; Weisberg and Prinz 1998; Weisberg et al. 2006; Lehner et al. 2010, 2011, 2012a). The MSN are distinct compositionally from the chondrules and they are essentially spheroidal objects composed primarily of kamacite (αFe-Ni) and troilite (FeS), with other sulfides including oldhamite (CaS), niningerite ([Mg,Fe,Mn]S), djerfisherite ($[K,Na]_6[Fe,Ni,Cu]_{25}S_{26}Cl$), caswellsilverite ($NaCrS_2$), and daubreelite ($FeCr_2S_4$). They typically contain schreibersite ($[Fe,Ni]_3P$), perryite ($[Fe,Ni]_5[Si,P]_2$), and silicate inclusions that consist of pyroxene, cristobalite, tridymite, roedderite ($[Na,K]_2[Mg,Fe]_5Si_{12}O_{30}$), and S-rich porous amorphous silica (Lehner et al. 2012a). Sahara 97072 has MSN that retain their spheroidal shape, contain both metal and sulfides, and are concentrically layered with intervening silicates (Figs. 2A and 2B). The MSN in ALH 84170 and LAR 06252 tend to be more homogeneous, i.e., all metal or all sulfide, and less spheroidal, although spheroidal layered MSN occur in these two meteorites as well.

EH3 chondrites also contain spheroidal chondrule-like objects that are difficult to classify as either pyroxene-rich silicate chondrules or MSN because they contain up to equal parts of silicates, sulfides, and kamacite in varied, gradational proportions (Figs. 2C–G). In other words, pyroxene-rich chondrules lacking sulfides and MSN lacking silicates are endmembers of a transitional series of spheroidal objects composed of mixtures of opaque and nonopaque minerals (Fig. 2). We estimate that approximately 41 vol% of Sahara 979072 consists of silicate chondrules and clasts, and approximately 37 vol% consists of MSN, mixed objects, and clasts of metal and sulfide (Table 1).

When viewed in transmitted light, material interstitial to large objects and clasts is opaque and undistinguishable from the metal and troilite. By combining transmitted and reflected light, the opaque matrix can be distinguished from metal, sulfides, and silicates (Fig. 1). In backscattered electron images, most matrix is hard to distinguish from chondrules and chondrule fragments except where accumulations are large enough for the granularity to be made visible by the fine-grained metal and sulfides (Figs. 3 and 4). These accumulations typically occur in physical depressions or embayments of large chondrules and clasts and other protected areas (Figs. 3A, 3B, 4A, 4B, 4E, and 4F) similar to the fine-grained material described in EH3s Yamato-691 and Allan Hills 81189 (Rubin et al. 2009). Some fine-grained material occurs as lumps or aggregates (Fig. 3C). We estimated the modal proportion of matrix to be approximately 21.5 vol% in Sahara 97072, approximately 17.4 vol% in ALH 84170, and approximately 18.7 vol% in LAR 06252.

TEM FIB sections were obtained in all three meteorites from the areas of large accumulations (e.g., Figs. 3B, 3D, 3F, and 4F) and areas of smaller dimension interstitial to chondrules, MSN, and large clasts. The mineral constituents are similar in either case. Our LA-ICPMS trace element analyses were performed on the accumulations of fine-grained material large enough to accommodate at least a 30 μm laser spot in Sahara 97072.

Matrix Mineralogy (TEM)

The EH3 matrix from the three meteorites is remarkably similar and consists almost entirely of four minerals. In order of abundance (based on point counting of TEM FIB sections), they are: 50–80 vol% enstatite, approximately 20–40 vol% cristobalite, <5–20 vol% kamacite and troilite (Fig. 5). The pyroxene is typically pure endmember enstatite, but ranges up to 3 at % ferrosilite. Cristobalite can be recognized by its pure SiO_2 composition and characteristic SAED

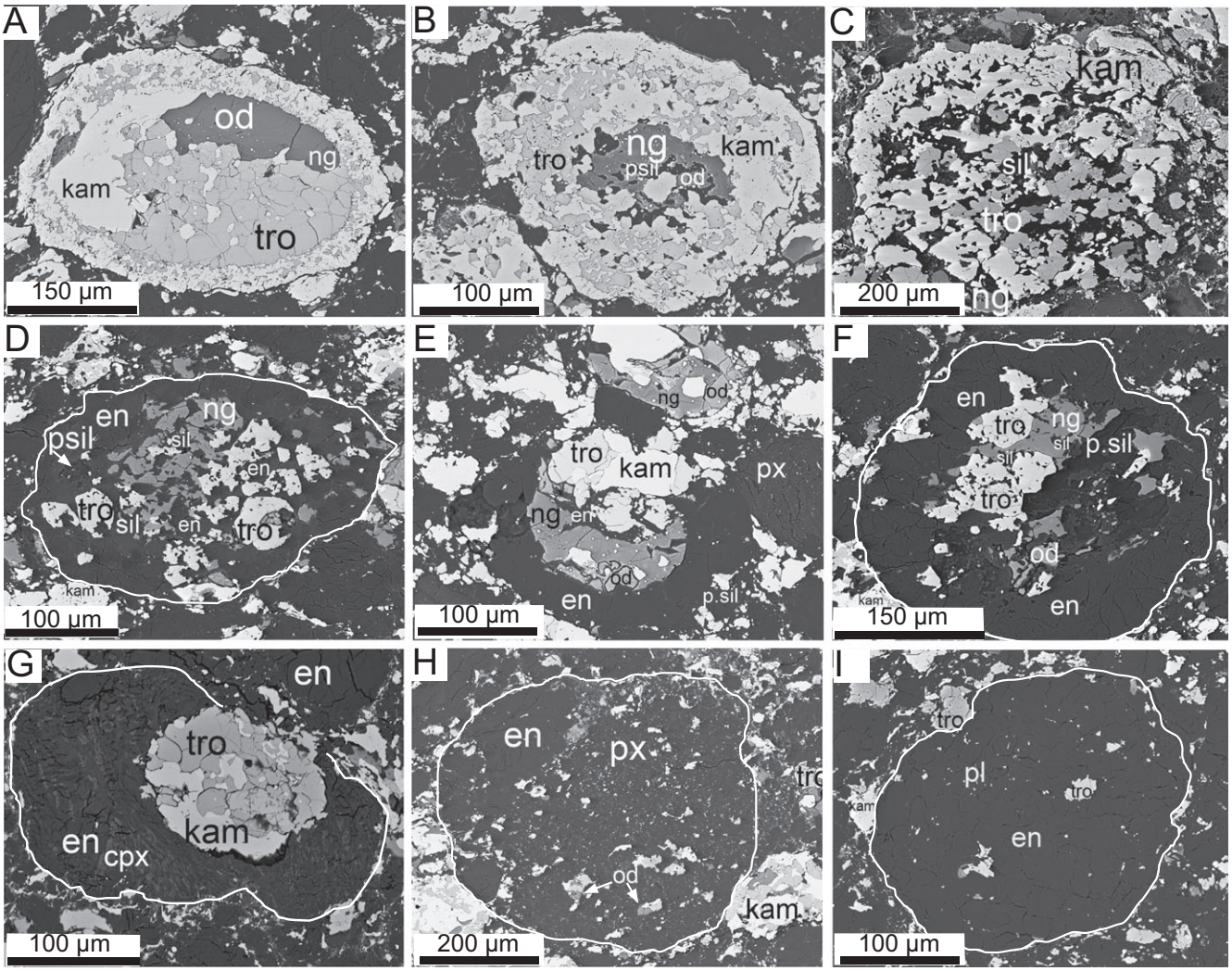

Fig. 2. BSE images of objects from Sahara 97072 illustrating the continuous series between MSN and ferromagnesian chondrules. A) Endmember MSN with a large core and distinct kamacite–troilite mantle. B) MSN containing porous silica inclusions within a niningerite/oldhamite core. C) MSN composed of kamacite and troilite with minor niningerite containing numerous silica-rich inclusions including porous silica. D) Silica-sulfide-rich chondrule composed of approximately equal opaque and nonopaque minerals where the silicates occur as inclusions within, and form a mantle around, the opaque minerals. E) Kamacite–troilite–niningerite nodule enclosed in an enstatite mantle and also containing enstatite inclusions in the core. Porous silica is adjacent to the enstatite mantle and nearby is an FeO-rich pyroxene grain. F) Opaque-rich chondrule with an enstatite mantle enclosing substantial porous silica, troilite, niningerite, and minor oldhamite. G) MSN engulfed in a pyroxene mantle. H) Ferromagnesian chondrule enclosing abundant sulfides and metal. I) Endmember ferromagnesian chondrule enclosing minor opaque minerals. px = pyroxene, cpx = clinopyroxene, od = oldhamite, ng = niningerite, psil = porous silica, sil = silica, pl = plagioclase, other abbreviations as in previous figures.

patterns. SAED patterns suggest the troilite is typically S-rich because the streaking of reflections implies Fe vacancy ordering consistent with pyrrhotite (Fig 5). The troilite typically contains Cr ranging from 1.4 up to 4 wt%, and just under 1 wt% Ti. Kamacite Ni concentration ranges from 4 to 6.5 wt% and Si concentration ranges from 2.5 to 4 wt%. After extensive investigation of the three meteorites, no olivine has been identified, although it is common in ordinary and carbonaceous chondrite matrices. Common minor minerals include: schreibersite, niningerite, oldhamite, keilite, sphalerite, augite, albite, and labradorite. C-rich spherules are common in all three meteorites (Fig. 6). EELS and HRTEM images indicate that the C spherules are amorphous. C-rich material also occurs as nonspheroidal patches and veins. Many of the submicrometer minerals are enclosed in amorphous SiO_2-rich material with variable concentrations of Al and Ca. Uncommon nanometer-scale magnetite particles occur in veins and voids in the ALH 84170

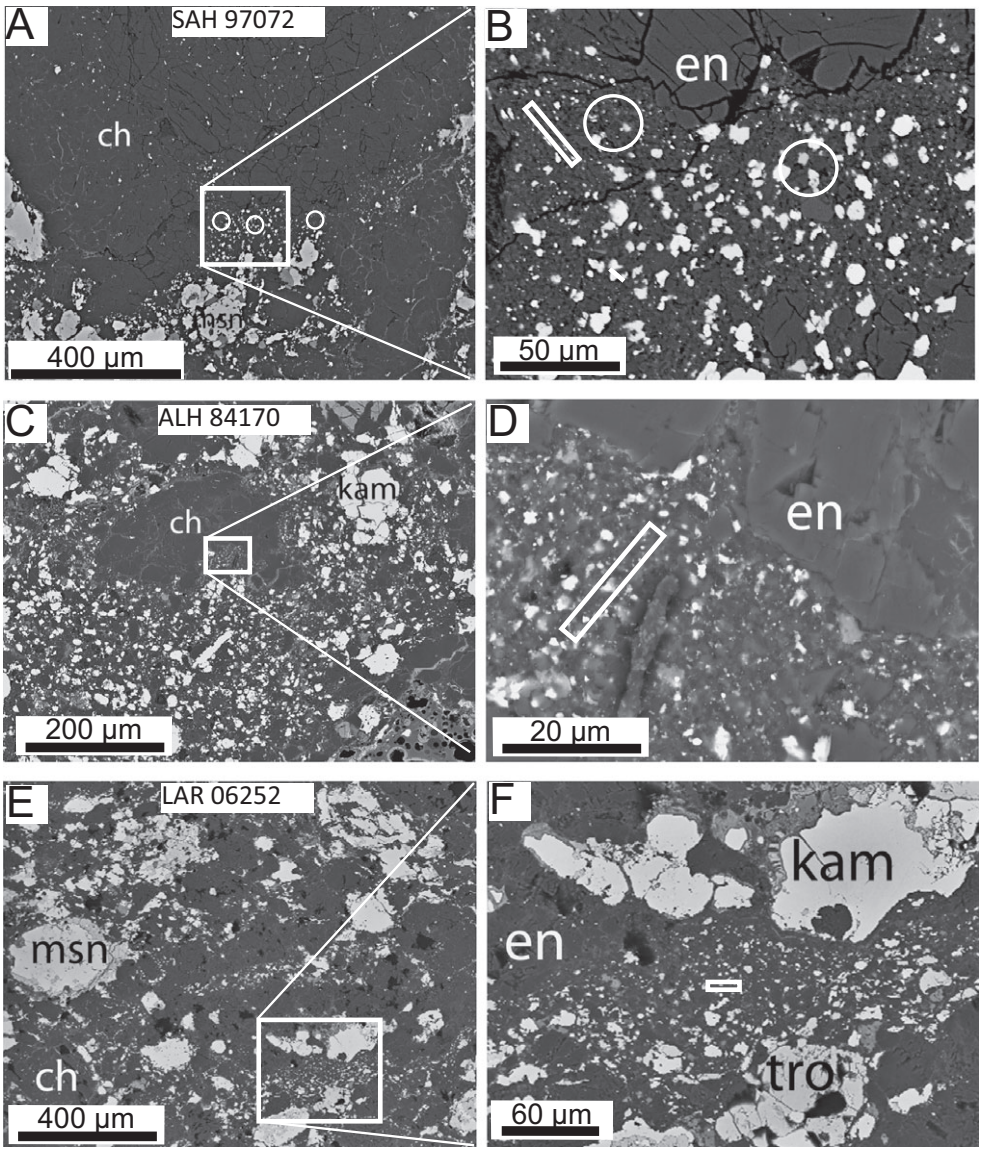

Fig. 3. Backscattered electron (BSE) images of EH3 matrix showing FIB locations (rectangles). A) Large chondrule from Sahara 97072 containing an embayment filled with fine-grained material. Circles represent areas chosen for LA-ICPMS analyses. B) Enlargement of area inside the white rectangle in (A) showing the texture of the area chosen for the ablation spots (circles) and FIB extraction (narrow rectangle). C) Low-magnification image of chondrule from ALH 84170 surrounded by fine-grained material or matrix lump. D) Enlargement of area inside rectangle in C showing FIB site. E) Low-magnification image of fine-grained material interstitial to chondrules and large clasts from LAR 06252. F) Enlargement of area inside rectangle in E showing location of FIB section. ch = chondrule, msn = metal-sulfide nodule. Other abbreviations as in previous figures.

matrix and embedded within cristobalite in LAR 06252 matrix.

Major and Minor Elements in Sahara 97072

Chondrite elemental compositions are commonly normalized to Si or Mg. However, thermal processing of the EH chondrules under high fS_2 fractionated Mg from Si through evaporation (Lehner et al. 2013b). Therefore, to avoid the appearance of systematic enrichments and depletions, we normalized to Al, which is refractory and presumably did not experience significant evaporative loss. Normalized to Al, the range of measurements (error bars, Fig. 7) for major and minor element bulk composition of Sahara 97072 overlaps CI chondrites, with the exception of Si which is enriched and Mg which is depleted. The bulk atomic Ca/Al ratio from ICP-AES is 0.73 compared to the CI ratio of 0.72 (Lodders 2003), indicating Ca is not significantly fractionated from Al in the bulk.

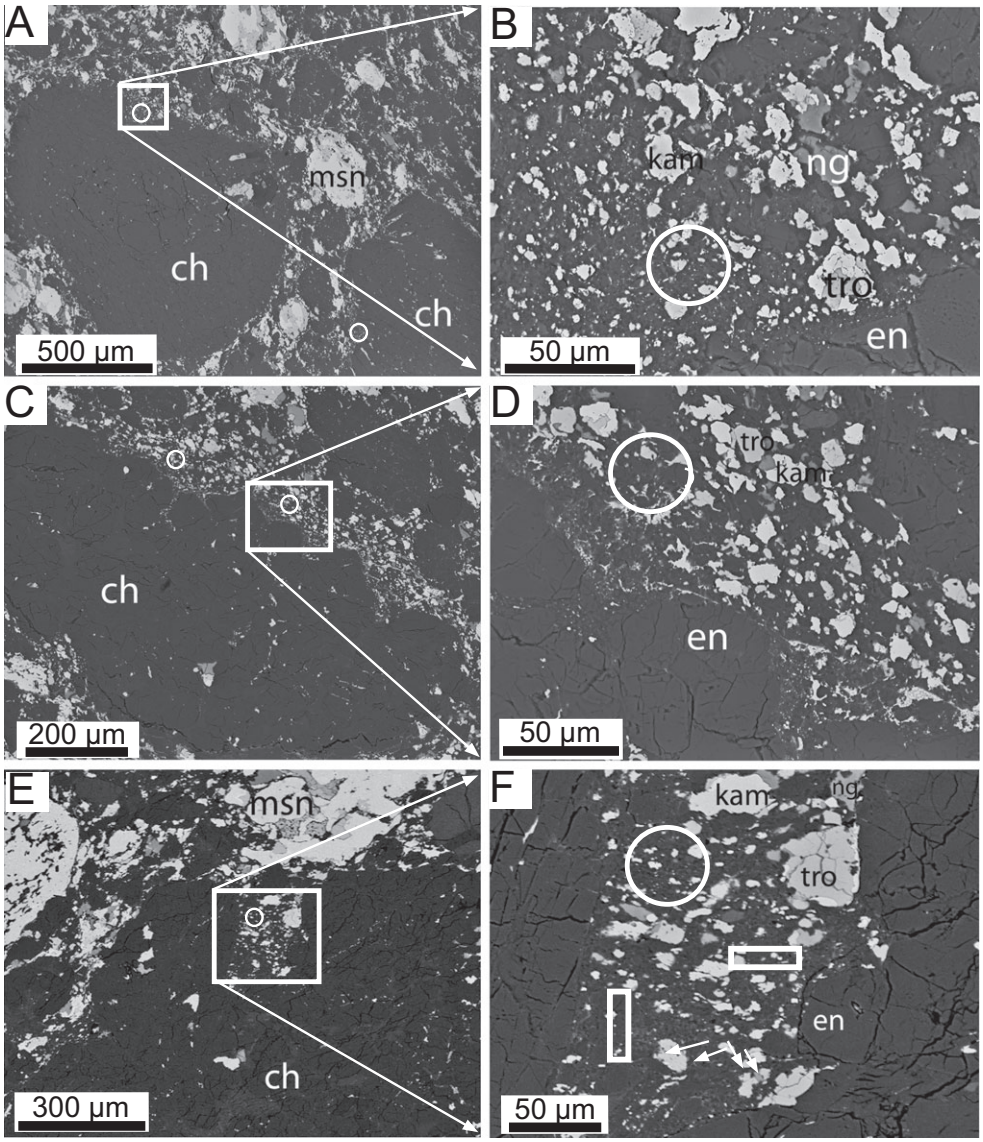

Fig. 4. BSE images of Sahara 97072 matrix areas chosen for LA-ICPMS analyses (circles) and FIB locations (rectangles). A) Large chondrule surrounded by fine-grained material, metal-sulfide nodules, other chondrules and clasts. B) Enlargement of area inside the white rectangle in (A) showing the chondrule embayment and the texture of the area chosen for the ablation spot. C) Low-magnification image of chondrule surrounded by fine-grained material indicating the location of the LA-ICPMS analyses. D) Enlargement of area inside rectangle in C. E) Low-magnification image of a chondrule embayment containing fine-grained material sampled by LA-ICPMS. F) Enlargement of area inside rectangle in E showing the laser-ablation spot and locations of FIB sections. Abbreviations as in previous figures.

However, the mean atomic Ca/Al for matrix and chondrules is 0.29 and 0.35, respectively. The Ca/Al ratios for chondrules and matrix are low because neither contains significant amounts of the predominant Ca-bearing mineral, oldhamite (CaS), most of which occurs within MSN and as coarse-grained clasts.

To facilitate compositional comparisons among matrix, chondrules, and bulk meteorite, it is useful to summarize which minerals contain the major and minor elements. Most Fe occurs in kamacite within metal-sulfide nodules, as clasts, and as grains in the matrix rather than as FeO in silicates. Al occurs primarily in albite and albitic glass in the chondrule mesostasis and fine-grained matrix. Most Si occurs in enstatite, amorphous silica, and silica polymorphs, and Mg is mainly in enstatite with less in olivine and niningerite. The enstatite and silica occur in chondrules, as clasts, and in the matrix, whereas olivine occurs only in certain chondrules. S is predominantly in troilite, niningerite,

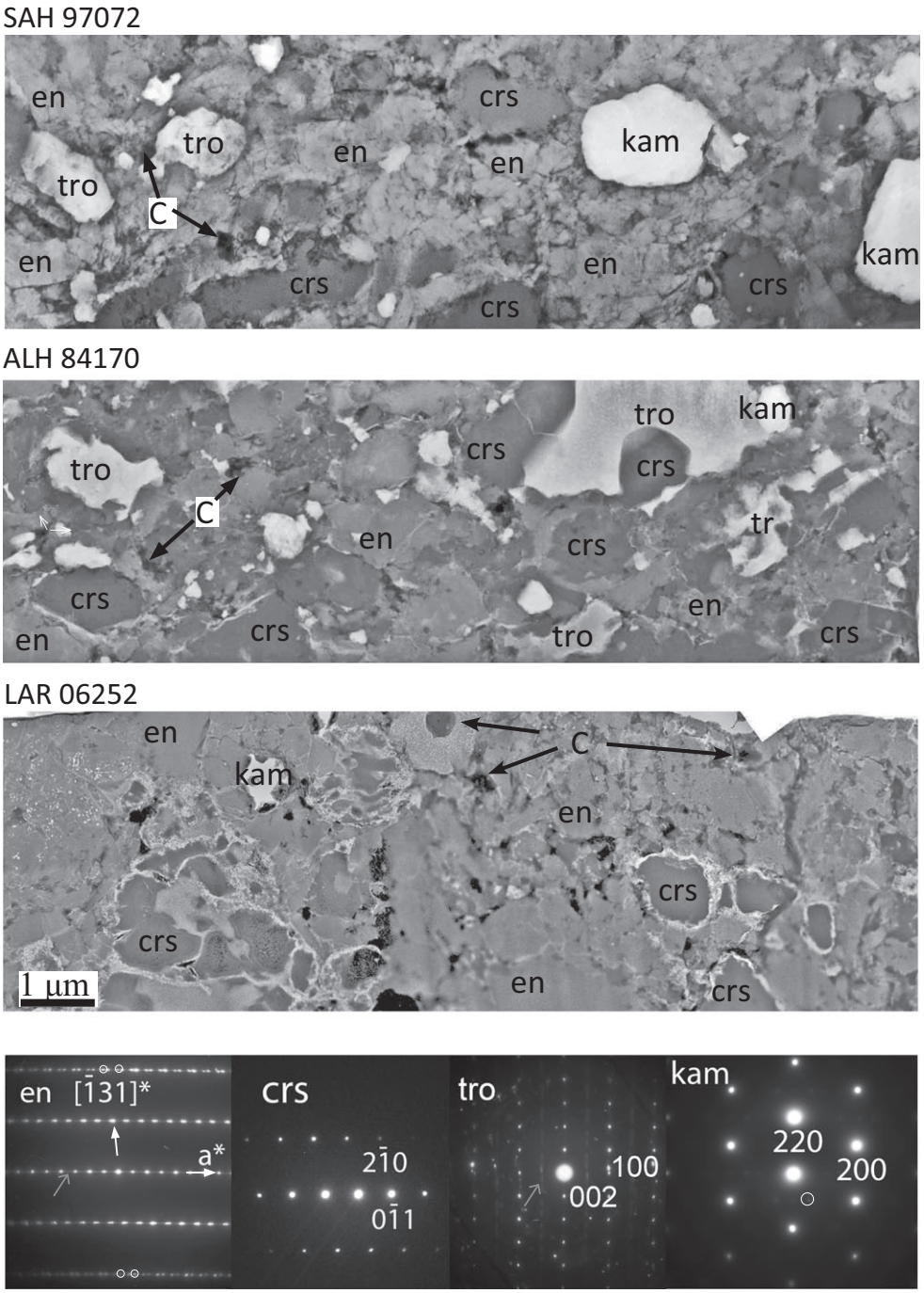

Fig. 5. High-angle, annular dark-field STEM images of EH3 matrix and representative SAED patterns of the primary mineral components: enstatite, cristobalite, troilite, and kamacite. Matrix from all three meteorites contains essentially the same minerals in similar proportions. The SAED patterns of these minerals typically indicate nanoscale complexity. Enstatite, here indexed as clinoenstatite, is twinned and contains stacking faults (ortho- and clinoenstatite) as its SAED pattern shows extra reflections (white circles) and streaking of reflections (gray arrow). Troilite SAED patterns typically show streaking (gray arrow) indicative of Fe vacancy ordering suggesting the occurrence of $Fe_{1-x}S$ (pyrrhotite). Kamacite SAED patterns commonly have faint reflections (white circle) possibly indicating Ni ordering. C = amorphous carbon. Other abbreviations as in previous figures.

and oldhamite, which occur in the chondrules, metal-sulfide nodules, as coarse-grained clasts, and as fine grains within the matrix.

The matrix everywhere is relatively constant in Si and Mg concentrations. However, there is inhomogeneity in the distribution of Fe, Mn, Ca, S, and

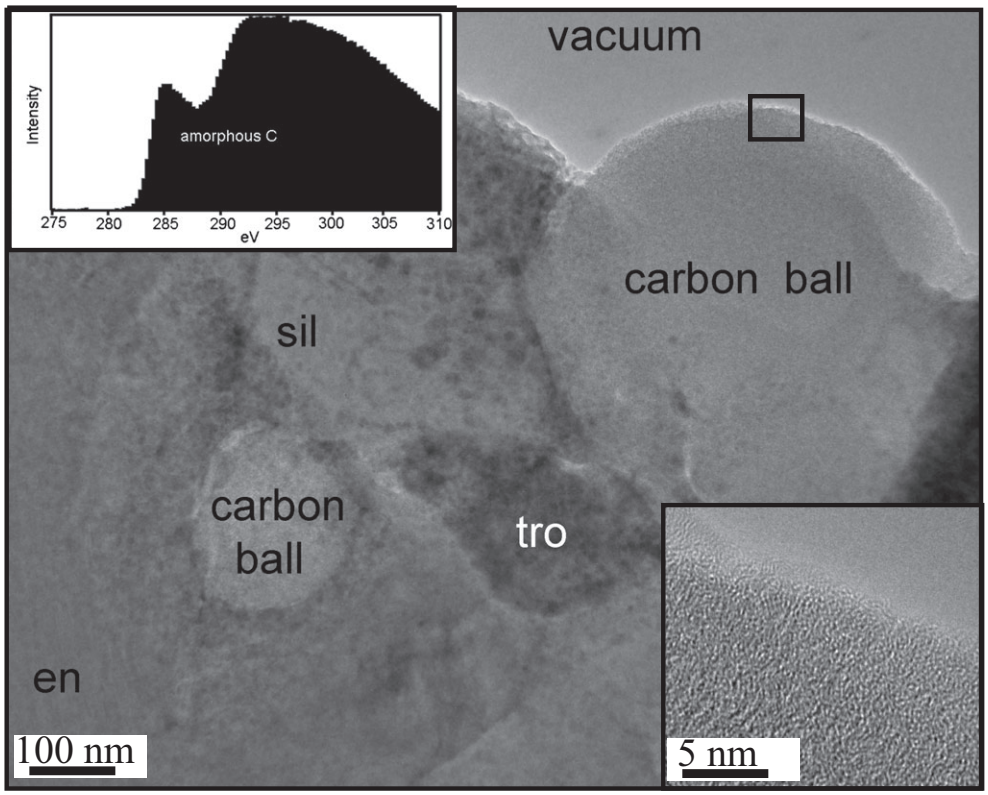

Fig. 6. Bright-field TEM image showing C balls from LAR 06252. Upper left and lower right insets are the EELS data and HRTEM image, respectively, consistent with amorphous C. Sil = silica, other abbreviations as in previous figures.

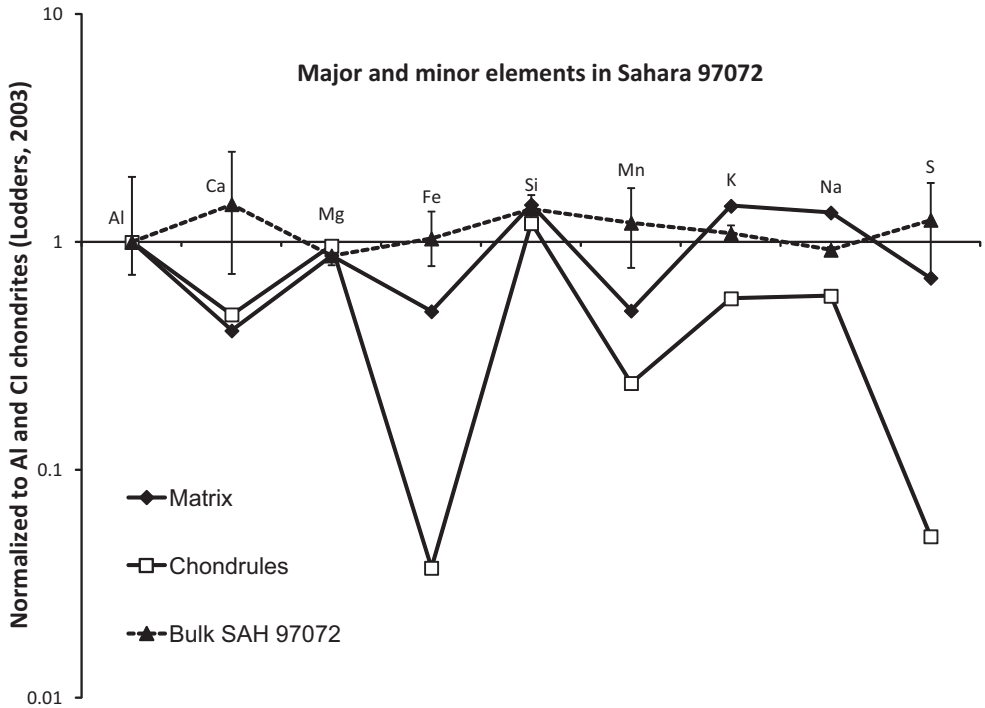

Fig. 7. Plot of selected major and minor element concentrations in Sahara 97072 matrix, chondrules, and bulk meteorite. Error bars on bulk values represent the range of measurements. All concentrations are normalized to Al and CI chondrite compositions.

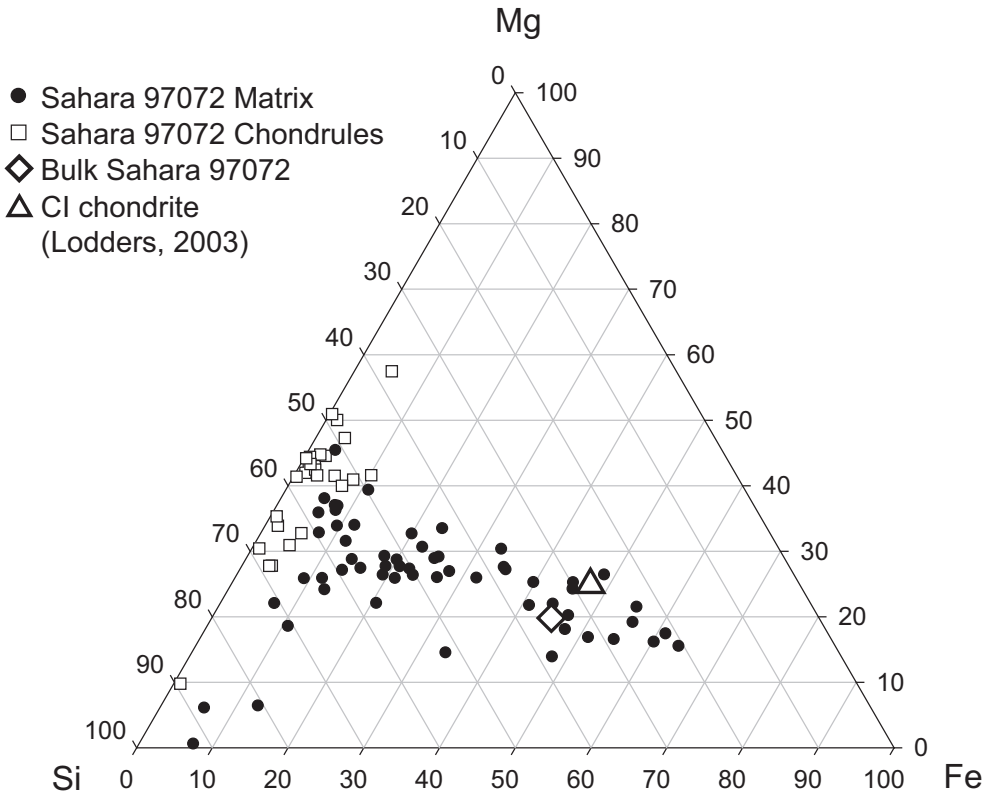

Fig. 8. Mg-Si-Fe ternary diagram including both EMPA and LA-ICPMS analyses for Sahara 97072 matrix and chondrules. The more Fe-rich matrix data tend to be from the LA-ICPMS analyses, which included more metal and sulfide fragments. The large diamond represents the mean composition of bulk Sahara 97072. The triangle represents CI chondrites.

Al, reflecting the uneven occurrence of kamacite, troilite, oldhamite, and plagioclase. When normalized to Al and compared to CI chondrites, the matrix is enriched in Si, K, and Na and depleted in Ca, Fe, and Mn. The chondrules are depleted in Ca, Fe, Mn, K, Na, and S (Fig. 7). The compositions of chondrules, matrix, and bulk meteorite are distinct from one another (Fig. 8), with chondrules richer in Mg and matrix richer in Fe and Si. The most Fe-rich matrix has similar Fe, Si, and Mg concentrations as the bulk meteorite.

Trace Element Chemistry

The ranges of most of our bulk trace element measurements overlap with those of Wasson and Kallemeyn (1988) for EH chondrites, although for some elements the overlap is within 15% of their values. Values are higher for Th, U, Pr, La, Ce, and Pb, and lower for V, Pt, Ni, Pd, Au, Na, Ge, Te, Se, Cd, Tl, and C (Fig. 9; Table 2). When normalized to Al and compared to CI chondrites (Lodders 2003), the bulk meteorite is enriched in all REE, with greater enrichment in light REE: La, Ce, and Pr and a flat pattern for the other REE (Fig. 10). It is also enriched in refractory lithophile elements: Th, U, La, Ce, and Ba; moderately volatile elements: As, Ag, Rb, and Pb; and depleted in siderophile elements Pt, Ni, and Pd; volatile elements Ge, Sn, Te, Se, Cd, Tl, O, and C; and the refractory lithophile element V. The ranges of measurements for other elements overlap values for CI chondrite composition except for a modest enrichment in Si and Co and depletion in Mg.

The matrix values, when normalized to CI chondrites, are relatively close to unity for refractory lithophile elements and enriched for many moderately volatile to volatile elements, with a notable enrichment in Au (Fig. 11A; Table 3). In contrast, the chondrules are enriched in most refractory lithophile elements, highly depleted in siderophile elements, and somewhat depleted in moderately volatile elements except for Na, Rb, and Cs. However, when normalized to Al and CI chondrites (Fig. 11B; Table 3), matrix is depleted in most refractory elements and enriched in Si relative to chondrules, whereas the chondrules are enriched only in Th and depleted in Ti, Nb, Ca, Yb, and siderophile elements.

DISCUSSION

Sahara 97072, ALH 84170, and LAR 06252 are among the most primitive EH3s known (Weisberg and

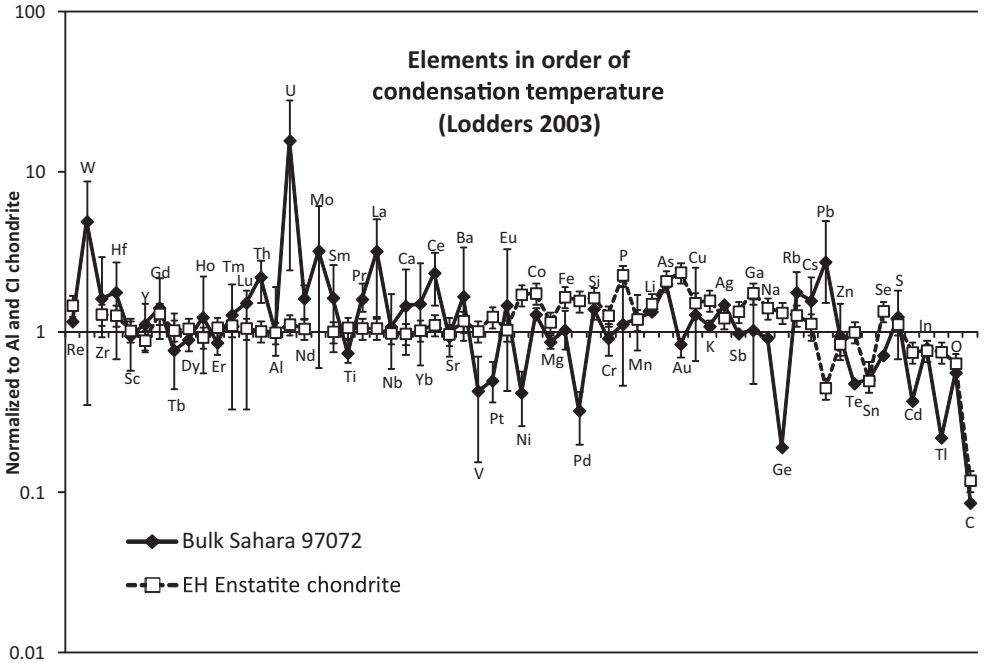

Fig. 9. Plot of the bulk Sahara 97072 composition normalized to Al and CI. The bars represent the range of measurements, and the diamond symbols represent the means. For comparison, EH data from Wasson and Kallemeyn (1988) are plotted in the open squares. 15% error bars are shown on their data to indicate the extent of overlap with our data ranges.

Prinz 1998; Weisberg et al. 2006; Komatsu et al. 2011; Quirico et al. 2011). Presolar silicates in Sahara 97072 (Ebata et al. 2006) indicate that at least a minor portion of matrix (<14 ppm) consists of primitive, relatively unprocessed material, i.e., they suggest the matrix has not been significantly altered since accretion. However, evidence for terrestrial weathering, in ALH 84170 and LAR 06252 exists as magnetite particles. All trace element analyses were measured in Sahara 97072, which is the least weathered meteorite. Nevertheless, weathering in a hot desert environment has been associated with enrichments of certain elements from the soil including Li, Sr, Mo, Ba, Pb, and U (Hezel et al. 2011); some of these enrichments are seen in Sahara 97072.

For most chondrite groups, comparison of major and trace element concentrations in matrix, chondrules, and the bulk meteorite can potentially provide genetic information. Matrix composition similar to chondrules implies that both, or their precursors, were subjected to similar processes. If matrix contains a large proportion of chondrule fragments, but has a distinct trace element signature, it suggests a portion of the matrix originated separately and was mixed with chondrules or that the chondrule fragments underwent chemical processing. Complementary chondrule and matrix compositions suggest that chemical transfer occurred from one to the other, or that both derived from the nebula by sampling different regions or perhaps the same region at different times (Hezel and Palme 2008, 2010). In EH3 chondrites, MSN must be considered as a distinct trace element reservoir to assess the complementary relation among components.

The origin of the MSN remains controversial. One idea is that the niningerite and oldhamite, which commonly occur in MSN cores, indicate a condensation origin for these objects (Lin and El Goresy 2002). Other studies indicate that MSN have been melted and experienced secondary processing in the nebula (Lehner et al. 2010; Horstmann et al. 2014). We interpret the observation of intermediate objects containing mixtures of metal, sulfides, and silicates (Figs. 2D–G) as evidence for secondary processing of MSN and that all the components of EH3 chondrites experienced the same environment. We hypothesize that compositional complementarity probably exists among the matrix, endmember MSN, and chondrules.

The EH3 matrix is distinct from other chondrite groups in that olivine, which is commonly the most abundant matrix mineral, is scarce or nonexistent contributing to low Mg/Si ratios. In addition, the EH3 silicates have much lower FeO content, the matrix contains abundant cristobalite, and there are no hydrous minerals. In the porous or clastic matrix from ordinary chondrites, the pyroxenes range from $En_{98\text{-}70}$,

Table 2. Bulk concentration data for Sahara 97072 (ppm).

Element	Mean	Max	Min	Stdev	CI	Ave EH[a]	Element	Mean	Max	Min	Stdev	CI	Ave EH[a]
Re	0.06				0.04	0.05	Co	825	902	786	41	502	840
W	0.6	1.0	0.04	0.45	0.09		Mg	106,227	116,938	96,517	6726	95,870	106,000
Zr	8.2	15.0	4.7	3.5	4.0	4.9	Fe	240,417	318,000	183,167	46,476	182,800	290,000
Hf	0.3	0.4	0.1	0.1	0.1	0.1	Pd	0.2	0.3	0.2	0.07	0.6	0.9
Sc	7	9	4	2	5.83	5.70	Si	189,445	219,029	163,402	22,500	106,500	167,000
Y	2.2	2.9	1.5	0.7	1.53	1.30	Cr	3024	3733	2350	393	2590	3150
Gd	0.4	0.6	0.2	0.1	0.2	0.2	P	1313	2240	546	631	920	2000
Tb	0.04	0.06	0.02	0.02	0.04	0.04	Mn	2946	4189	1880	829	1910	2200
Dy	0.27	0.32	0.23	0.03	0.24	0.24	Li	3				1.5	2.1
Ho	0.09	0.16	0.04	0.04	0.06	0.05	As	4				1.7	3.5
Er	0.18	0.23	0.15	0.03	0.16	0.17	Au	0.2	0.2	0.1	0.02	0.1	0.3
Tm	0.04	0.06	0.01	0.02	0.02	0.03	Cu	208	410	108	92	127	185
Lu	0.05	0.06	0.01	0.02	0.02	0.02	K	735	800	704	30	530	800
Th	0.09	0.11	0.06	0.02	0.03	0.03	Ag	0.4				0.2	0.2
Al	10,803	20,869	7782	4545	8500	8100	Sb	0.2				0.2	0.2
U	0.17	0.30	0.03	0.13	0.01	0.01	Ga	12	20	6	5	10	16
Nd	0.9	1.1	0.7	0.3	0.5	0.5	Na	5885	6100	5697	117	5010	6800
Mo	4	8	1	3	1		Ge	8				33	42
Sm	0.3	0.5	0.1	0.1	0.1	0.1	Rb	5	7	4	1	2	3
Ti	415	504	363	48	440	450	Cs	0.4	0.5	0.2	0.1	0.2	0.2
Pr	0.19	0.24	0.16	0.03	0.09	0.09	Bi	5				0.1	0.1
La	0.9	1.5	0.4	0.3	0.2	0.2	Pb	9	16	5	4	3	1
Nb	0.4	0.6	0.2	0.1	0.3	0.3	Zn	374	595	266	130	310	250
Ca	16,879	28,702	8397	8022	9070	8500	Te	1				2	2
Yb	0.3	0.6	0.1	0.2	0.2	0.2	Sn	1	1	1	0.16	2	1
Ce	1.9	2.5	1.2	0.4	0.6	0.7	Se	18				20	26
Sr	9	12	7	2	8	7	S	85,974	125,828	46,700	28,740	54,100	58,000
Ba	5	10	3	3	2	3	Cd	0.3				0.7	0.5
V	31	50	11	20	56	54	In	0.08				0.08	0.06
Pt	0.6	0.8	0.5	0.1	1.0	1.2	Tl	0.04				0.14	0.10
Eu	0.10	0.23	0.03	0.07	0.05	0.05	O	326,593	365,048	289,218	34,192	458,200	280,000
Ni	5678	7738	3510	1391	10,640	17,500	C	3852				35,180	4000

[a]Wasson and Kallemeyn (1988).

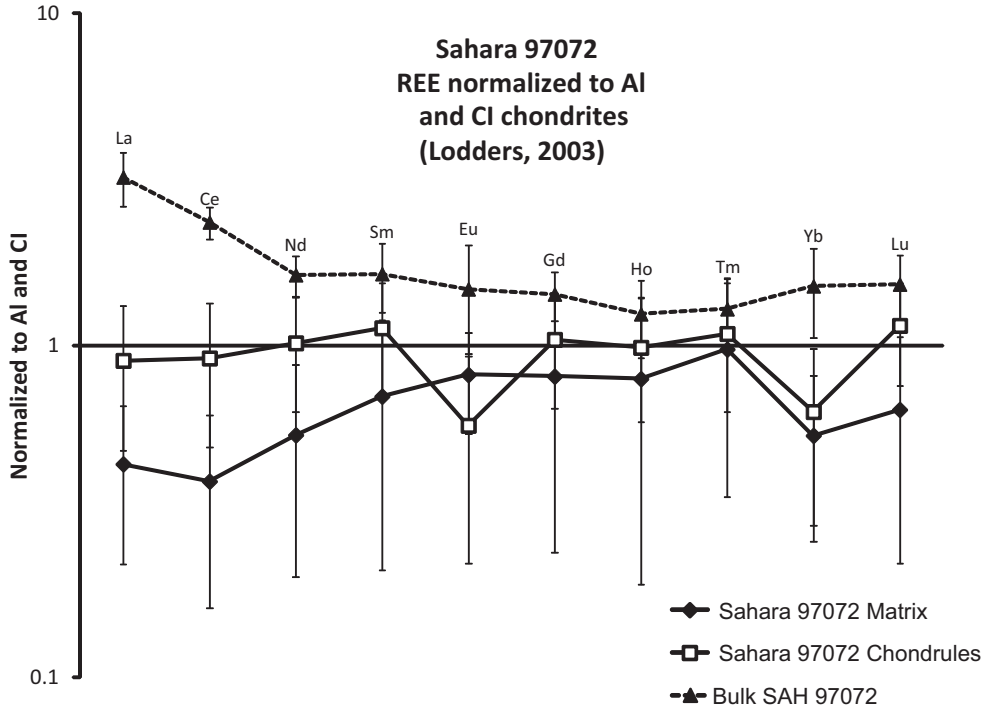

Fig. 10. Plot comparing selected REE concentrations normalized to Al and CI chondrites in Sahara 97072 matrix, chondrules, and bulk meteorite. Error bars correspond to relative error of the nonnormalized analyses applied to the normalized value.

and their matrices contain carbonates and hydrous minerals including calcite; whitlockite; and, in Semarkona (LL3), smectite (Alexander et al. 1989; Brearley and Jones 1998). The low Mg/Si ratios, low FeO silicates, and anhydrous minerals such as niningerite and oldhamite represent considerably different chemical trends in EH3 matrix than in ordinary or carbonaceous chondrites.

Ca, Al, and Fe Distribution

Bulk major and minor element concentrations in Sahara 97072 are similar to CI when normalized to Al (Fig. 7), indicating Ca is not significantly fractionated from Al in the bulk meteorite. However, Ca is depleted in matrix and chondrules relative to the bulk because it mainly occurs in oldhamite located in MSN and as large clasts. The oldhamite probably formed by sulfidation of Ca-bearing pyroxene in chondrules (Lehner et al. 2013a, 2013b) that were later disaggregated. Similar reasoning explains the depletion of Mn in the matrix and chondrules relative to the bulk because it mainly occurs in large niningerite clasts (Fig. 7). The similar Ca/Al ratio of the chondrules and the matrix is compatible with a matrix composed primarily of chondrule fragments. However, only highly sulfidized chondrules (Lehner et al. 2013b) contain cristobalite in similar proportions to the matrix.

The pyroxene-dominated chondrules measured in this study are depleted in Fe and siderophile elements (Fig. 11), consistent with loss of metal or formation from precursors after the proposed silicate-metal fractionation (Larimer and Wasson 1988a, 1988b). The matrix concentration of Fe (Fig. 8) results from its 15 to 20 vol% metal and troilite fragments (Table 1). The high Fe content of the bulk meteorite reflects the numerous MSN.

Explanation of Trace Element Distribution

The bulk trace element concentrations show that most refractory elements are not significantly fractionated from one another, consistent with the Ca/Al ratio. Exceptions are enrichments in Th, U, Mo, Ba, and Pb, which are probably associated with desert terrestrial weathering similar to that in meteorites from the United Arab Emirates (Hezel et al. 2011), and W enrichment, which only occurs in the results from acid-digested aliquots that may have been contaminated by tungsten carbide during pulverization.

Matrix and chondrule trace element concentrations are noncomplementary without the MSN trace element signature (Figs. 10 and 11;

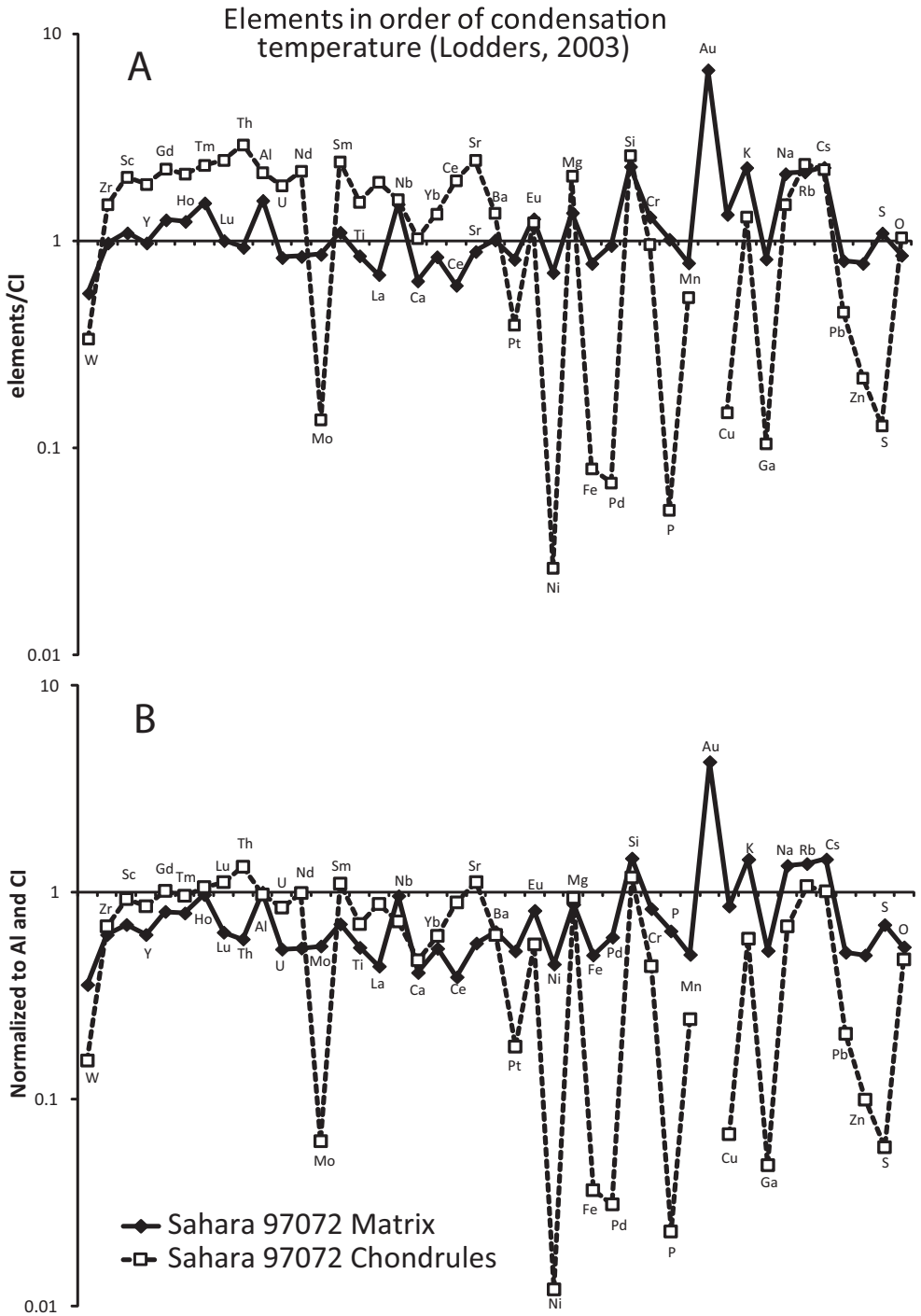

Fig. 11. Plots contrasting the trace element signatures of chondrules with matrix in Sahara 97072. A) Plot of element concentrations divided by concentration in CI chondrites with no normalizing element. B) Plot of element concentrations normalized to Al and divided by CI chondrites.

Table 3). Relative to matrix, the chondrules are enriched by a factor of 1.5–3 in all refractory lithophile elements except Nb and Eu (Fig. 12). The ratios of most pairs of refractory lithophile elements are remarkably similar in the chondrules and matrix, respectively, which suggests that the silicate portion of the matrix might consist primarily of chondrule fragments. However, our TEM observations of the

Table 3. Concentration of elements in matrix and chondrules (ppm) of Sahara 97072.

	Matrix				Chondrules			
Element[a]	Mean	Max	Min	Stdev	Mean	Max	Min	Stdev
Mg	120,000	177,000	29,800	34,900	188,000	272,000	35,800	63,000
Al	9440	23,900	2400	5000	18,700	66,000	870	17,600
Si	196,000	382,000	118,000	53,200	272,000	327,000	240,000	23,000
P	939	1640	260	400	46	193	8	62
S	96,900	208,000	16,500	50,000	12,000	27,000	4690	6470
Ca	6280	23,900	2160	4940	9470	39,600	1040	12,500
Sc	6	12	4	2	12	27	4	6
Ti	374	753	162	147	678	2300	127	652
Cr	3390	9580	1020	1760	2490	4180	492	998
Mn	1950	7940	348	1880	960	1340	600	254
Fe	231,000	423,000	61,400	91,300	20,100	53,700	1840	14,800
Ni	7510	25,200	2230	5240	281	681	25	277
Cu	171	368	68	73	19	44	2	11
Zn	242	1620	31	326	68	236	8	73
Ga	8	24	2	5	1	2	1	1
Rb	5	10	2	2	5	15	2	4
Sr	7	31	2	7	19	95	1	28
Y	1	10	0.2	2	3	8	0.2	2
Zr	4	13	1	2	6	21	1	6
Nb	0.4	1.0	0.2	0.2	0.42	1.10	0.02	0.51
Mo	0.9	1.9	0.2	0.4	0.14	0.20	0.02	0.07
Pd	0.6	1.5	0.1	0.5	0.04	0.08	0.02	0.03
Cs	0.4	1.0	0.2	0.2	0.4	1.3	0.1	0.5
Ba	2.3	5.6	0.9	1.5	3.5	16.8	0.9	5.1
La	0.2	0.7	0.0	0.2	0.4	1.4	0.03	0.4
Ce	0.4	2.0	0	0.4	1.2	4.1	0.02	1.1
Nd	0.4	2.2	0.1	0.5	1.0	2.4	0.04	0.8
Sm	0.2	0.9	0.01	0.23	0.4	0.7	0.02	0.3
Eu	0.1	0.1	0.02	0.04	0.1	0.3	0.01	0.1
Gd	0.3	1.2	0.03	0.35	0.4	1.1	0.07	0.3
Ho	0.1	0.4	0.01	0.10	0.1	0.3	0.02	0.1
Tm	0.04	0.15	0.01	0.05	0.1	0.1	0.01	0.05
Yb	0.1	0.53	0.03	0.1	0.2	0.7	0.03	0.2
Lu	0.03	0.14	0.01	0.04	0.1	0.1	0.01	0.04
W	0.05	0.15	0.01	0.03	0.0	0.1	0.01	0.03
Pt	0.8	2.0	0.4	0.47	0.4	0.4	0.35	0.1
Au	1.0	3.8	0.2	1.57	b.d.	b.d.	b.d.	b.d.
Pb	2.1	7.8	0.7	1.67	1.2	2.3	0.37	0.6
Th	0.030	0.097	0.004	0.021	0.1	0.2	0.01	0.1
U	0.012	0.04	0.002	0.010	0.0	0.1	0.01	0.02
O (EMP)	321,000	439,000	197,000	67,000	470,000	532,000	398,000	36,800
Na	10,300	18,700	1550	4340	7520	34,700	160	10,800
K	1160	1890	40	432	760	2750	70	941

[a]In order of 50% condensation temperature (Lodders 2003). For Al, Ca, Mg, Fe, Si, Mn, K, Na, S, and O, the values are the means of the combined LA-ICPMS and EMP results. The trace element values are the means of the LA-ICPMS results.

matrix show that the nonopaque material consists of approximately 55 vol% enstatite and up to 45 vol% cristobalite. The high proportion of cristobalite in the matrix does not typically occur in the measured pyroxene-rich chondrules where it is a minor phase commonly found in the mesostasis (Kimura et al. 2005). Abundant cristobalite does occur in the subset of sulfidized chondrules (Lehner et al. 2013b). The matrix depletion in refractory lithophile elements could result from addition of metal, sulfides, and cristobalite to the composition of the pyroxene-rich chondrule fragments.

The refractory element ratios and abundant cristobalite are consistent with the silicate portion of

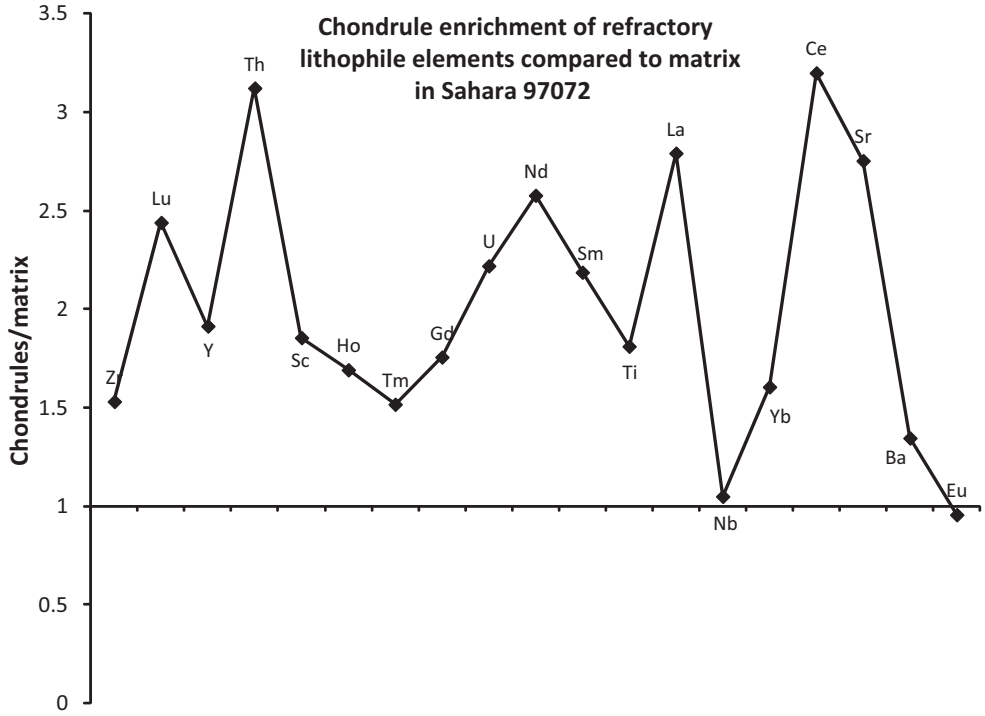

Fig. 12. Plot of refractory lithophile element concentrations in Sahara 97072 chondrules divided by their concentrations in the Sahara 97072 matrix.

the matrix consisting of a significant portion of sulfidized chondrule fragments. In sulfidized chondrules olivine, enstatite, and Ca-bearing pyroxene were partly replaced by niningerite, oldhamite, and fine-grained cristobalite. Those chondrules and chondrule fragments containing a larger portion of sulfidation products are enriched in volatiles and depleted in Mg and Ca as niningerite and oldhamite tend to be lost from spinning chondrules (Lehner et al. 2013b). Refractory lithophile elements are substantially enriched in oldhamite (Larimer and Ganapathy 1987; Crozaz and Lundberg 1995; Gannoun et al. 2011), and some are near CI concentration in niningerite (Fig. 13; Tables 4 and 5), suggesting these elements follow Ca and, to a lesser extent, Mg during sulfidation. As niningerite and oldhamite typically occur as grains greater than 5 μm across, they are underrepresented in our matrix analyses. Their low concentrations together with the abundant cristobalite can account for matrix depletion in refractory lithophile elements. The matrix enrichment in moderately volatile elements is consistent with measurements of highly sulfidized chondrules (Lehner et al. 2013b).

Sulfidized chondrules are a subset of the typical EH3 ferromagnesian chondrules that experienced extensive thermal, and gas–solid processing under high fS_2. Considering the potential complementary relation between the matrix, chondrules, and MSN, and the mixing relation between MSN and silicate chondrules, it is likely that these components were processed in a single environment that resulted in different Ca/Al ratios as chemical transfer (e.g., Ca) occurred between components. Ca/Al complementarity for CV chondrules and matrix resulting from chemical transfer in a common formation environment was proposed by Hezel and Palme (2008). The highly unequilibrated minerals and spheroidal shape of the MSN and chondrules, including highly sulfidized chondrules (Lehner et al. 2013b), suggest a nebular environment as opposed to a parent body setting.

CONCLUSIONS

The matrix of EH3 chondrites SAH 97072, ALH 84170, and LAR 06252 is composed almost entirely of enstatite, cristobalite, troilite, and kamacite in order of abundance. All three matrices contain amorphous C-rich spherules. The major and trace element composition of bulk Sahara 97072 is unique, but most element concentrations are within an order of magnitude from CI chondrite values. Exceptions are depletion in C and enrichment of U. The matrix of Sahara 97072 is depleted in refractory elements and

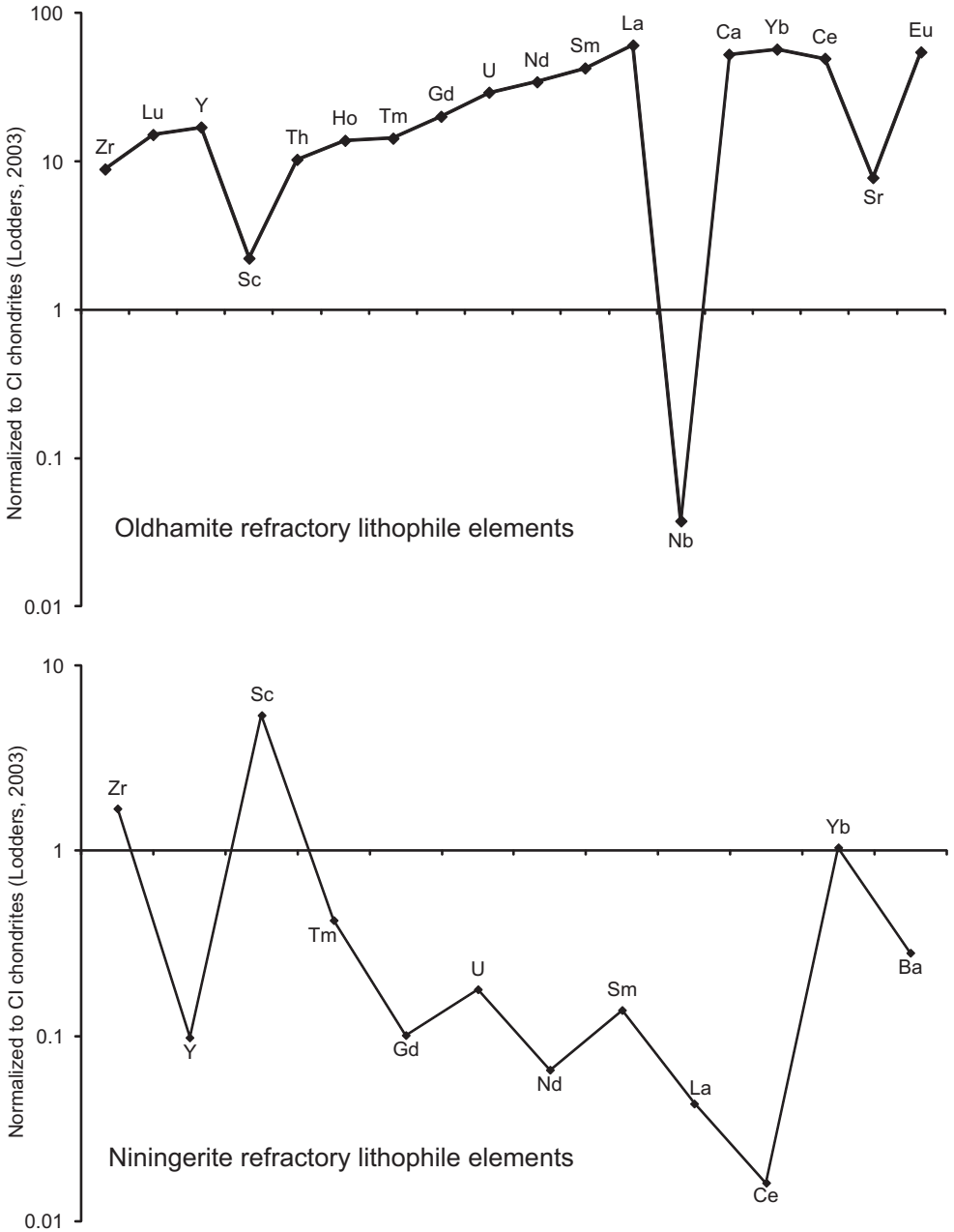

Fig. 13. Refractory lithophile element signatures of Sahara 97072 oldhamite and niningerite. A) Plot of oldhamite concentrations normalized to CI chondrites. B) Plot of niningerite concentrations normalized to CI chondrites.

enriched in moderately volatile elements compared to the pyroxene-dominated chondrules, and this relation may be complementary when the abundant MSN are considered. TEM observations of all three meteorites show that the matrix silicates are a nearly equal mixture of cristobalite and enstatite. The matrix, chondrules, and MSN probably formed in a nebular environment that experienced extensive thermal, and gas–solid processing under high fS_2 resulting in partial sulfidation of silicates. Because each of these components reacted with the same reservoir, they evolved unique, but probably complementary, Ca/Al ratios. The matrix composition and mineral proportions can be understood if matrix consists primarily of debris from highly sulfidized and subsequently disaggregated chondrules that had lost most of their oldhamite and niningerite.

Table 4. Oldhamite LA-ICPMS analysis (Sahara 97072).

Element[a]	Oldhamite ppm	CI ppm	element/CI
Zr	35.2	4.0	8.9
Sc	13	5.8	2.2
Y	26.1	1.5	17.1
Gd	4.0	0.20	20.2
Ho	0.78	0.056	13.9
Tm	0.34	0.024	14.3
Lu	0.36	0.024	15.2
Th	0.32	0.031	10.3
Al	194	8500	0.023
U	0.25	0.008	29.3
Nd	15.7	0.46	34.4
Mo	0.05	1.0	0.049
Sm	6.2	0.15	42.7
Ti	9	440	0.0
La	14.1	0.23	60.9
Nb	0.01	0.27	0.038
Ca	478,927	9070	52.8
Yb	9.3	0.16	57.2
Ce	30.8	0.62	49.5
Sr	60.3	7.7	7.8
Eu	3.0	0.05	54.8
Ni	268	10,640	0.025
Mg	5998	95,870	0.1
Cr	21	2590	0.008
P	293	920	0.3
Mn	1050	1910	0.5
Au	0.1	0.15	0.7
Cu	314	127	2.5
Ga	1	9.5	0.1
Cs	0.01	0.19	0.1
Pb	151	2.6	58.9
Zn	8	310	0.026
S	512,015	54,100	9.5

[a]In order of 50% condensation temperature (Lodders 2003).

Table 5. Niningerite LA-ICPMS analyses (Sahara 97072).

Element[a]	Niningerite (2)[b]ppm	CI ppm	Element/CI
W	0.01	0.089	0.1
Zr	6.7	4.0	1.7
Sc	32	5.8	5.4
Y	0.15	1.5	0.1
Gd	0.02	0.20	0.1
Tm	0.01	0.02	0.4
U	0.002	0.008	0.2
Nd	0.03	0.46	0.1
Mo	2.6	1.0	2.5
Sm	0.02	0.15	0.1
Ti	48	440	0.1
La	0.01	0.23	0.04

Table 5. *Continued*. Niningerite LA-ICPMS analyses (Sahara 97072).

Element[a]	Niningerite (2)[b]ppm	CI ppm	Element/CI
Ca	3274	9070	0.4
Yb	0.17	0.16	1.0
Ce	0.01	0.62	0.02
Ba	0.65	2.3	0.3
Mg	183,166	95,870	1.9
Fe	381,507	182,800	2.1
Cr	3526	2590	1.4
Mn	54,350	1910	28.5
Cu	227	127	1.8
Ga	3.0	9.5	0.3
Pb	0.50	2.6	0.2
Zn	438	310	1.4
S	368,237	54,100	6.8

[a]In order of 50% condensation temperature (Lodders 2003).
[b]Number of analyses.

Acknowledgments—We gratefully acknowledge the use of facilities within the LeRoy Eyring Center for Solid State Science at Arizona State University. We would also like to thank Peter Buseck for help in editing the initial version of this manuscript and for providing a platform to carry out this research. We appreciate the constructive reviews from Dominik Hezel and Neyda Abreu. We especially appreciate the expertise of Gordon Tam and Jason Ng for preparing some of our TEM FIB sections. This work was supported by the NASA grant NNX10AG48G.

Editorial Handling—Dr. Edward Scott

REFERENCES

Achterbergh E. V., Ryan C. G., Jackson S. E., and Griffin W. L. 2001. Appendix 3: Data reduction software for LA-ICP-MS. In *Laser ablation-ICP-MS in the earth sciences*, edited by Sylvester P. Quebec: Mineralogical Association of Canada. 243 p.

Alexander C. M. O'D. 2005. From supernovae to planets: The view from meteorites and interplanetary dust particles. In *Chondrites and the protoplanetary disk*, edited by Krot A. N., Scott E. R. D., and Reipurth B. San Francisco, California: Astronomical Society of the Pacific. pp. 972–1002.

Alexander C. M. O'D., Hutchison R., and Barber D. J. 1989. Origin of chondrule rims and interchondrule matrices in unequilibrated ordinary chondrites. *Earth and Planetary Science Letters* 95:187–207.

Brearley A. J. 1996. The nature of matrix in unequilibrated chondritic meteorites and its possible relationship with chondrules. In *Chondrules and the protoplanetary disk*, edited by Hewins R., Jones R. H., and Scott E. R. D. Cambridge: Cambridge University Press. pp. 137–152.

Brearley A. J. and Jones R. H. 1998. Chondritic meteorites. In *Planetary materials*, edited by Papike J. J. Washington, DC: Mineralogical Society of America. pp. 3-001–3-398.

Buseck P. R. and Hua X. 1993. Matrices of carbonaceous chondrite meteorites. *Annual Review of Earth and Planetary Sciences* 21:255–305.

Clayton R. N., Mayeda T. K., and Rubin A. E. 1984. Oxygen isotopic compositions of enstatite chondrites and aubrites. *Journal of Geophysical Research* 89:C245–C249.

Crozaz G. and Lundberg L. L. 1995. The origin of oldhamite in unequilibrated enstatite chondrites. *Geochimica et Cosmochimica Acta* 59:3817–3831.

Ebata S., Nagashima K., Itoh S., Kobayashi S., Sakamoto N., Fagan T. J., and Yurimoto H. 2006. Presolar silicate grains in enstatite chondrites (abstract #1619). 37th Lunar and Planetary Science Conference. CD-ROM.

Ebata S., Fagan T. J., and Yurimoto H. 2008. Identification of silicate and carbonaceous presolar grains by SIMS in the type-3 enstatite chondrite ALHA81189. *Applied Surface Science* 255:1468–1471.

Gannoun A., Boyet M., El Goresy A., and Devouard B. 2011. REE and actinide microdistribution in Sahara 97072 and ALHA77295 EH3 chondrites: A combined cosmochemical and petrologic investigation. *Geochimica et Cosmochimica Acta* 75:3269–3289.

Hamester M., Weiderin D., Wills J., Kerl W., and Douthitt C. B. 1999. Strategies for isotope ratio measurements with a double focusing sector þ eld ICP-MS. *Fresenius Journal of Analytical Chemistry* 364:495–497.

Hezel D. C. and Palme H. 2008. Constraints for chondrule formation from Ca-Al distribution in carbonaceous chondrites. *Earth and Planetary Science Letters* 265:716–725.

Hezel D. C. and Palme H. 2010. The chemical relationship between chondrules and matrix and the chondrule matrix complementarity. *Earth and Planetary Science Letters* 294:85–93.

Hezel D. C., Schluter J., Kallweit H., Jull T., Al Fakeer O. Y., Al Shamsi M., and Strekopytov S. 2011. Meteorites from the United Arab Emirates: Description, weathering, and terrestrial ages. *Meteoritics & Planetary Science* 46:327–336.

Horstmann M., Humayun M., and Bischoff A. 2014. Clues to the origin of metal in Almahata Sitta EL and EH chondrites and implications for primitive E chondrite thermal histories. *Geochimica et Cosmochimica Acta* 140:720–744.

Huss G. R. and Lewis R. S. 1995. Presolar diamond, SiC, and graphite in primitive chondrites: Abundances as a function of meteorite class and petrologic type. *Geochimica et Cosmochimica Acta* 59:115–160.

Huss G. R., Alexander C. M. O'D., Palme H., Bland P. A., and Wasson J. T. 2005. Genetic relationships between chondrules, fine grained rims, and interchondrule matrix. In *Chondrites and the protoplanetary disk*, edited by Krot A. N., Scott E. R. D. and Reipurth B. San Francisco, California: Astronomical Society of the Pacific. pp. 701–731.

Ikeda Y. 1989. Petrochemical study of the Yamato-691 enstatite chondrite (E3) IV: Descriptions and mineral chemistry of opaque-mineral nodules. *Proceedings of the NIPR Symposium on Antarctic Meteorites* 2:109–146.

Jacobsen S. B., Petaev M. I., Huang S., and Sasselov D. D. 2013. An isotopically homogeneous region of the inner terrestrial planet region (Mercury to Earth): Evidence from E. chondrites and implications for giant moon-forming impact scenarios (abstract #2344). 44th Lunar and Planetary Science Conference. CD-ROM.

Javoy M. 1995. The integral enstatite chondrite model of the Earth. *Geophysical Research Letters* 22:2219–2222.

Javoy M., Kaminski E., Guyot F., Andrault D., Sanloup C., Moreira M., Labrosse S., Jambon A., Agrinier P., Davaille A., and Jaupart C. 2010. The chemical composition of the Earth: Enstatite chondrite models. *Earth and Planetary Science Letters* 293:259–268.

Kaminski E. and Javoy M. 2013. A two-stage scenario for the formation of the Earth's mantle and core. *Earth and Planetary Science Letters* 365:97–107.

Keil K. 1968. Mineralogical and chemical relationships among enstatite chondrites. *Journal of Geophysical Research-Planets* 73:6945–6975.

Kimura M. 1988. Origin of opaque minerals in an unequilibrated enstatite chondrite, Yamato-691. *Proceedings of the NIPR Symposium on Antarctic meteorites* 1:51–64.

Kimura M., Weisberg M. K., Lin Y., Suzuki A., Ohtani E., and Okazaki R. 2005. Thermal history of the enstatite chondrites from silica polymorphs. *Meteoritics & Planetary Science* 40:855–868.

Komatsu M., Fagan T. J., Ozaki N., Mikouchi T., and Miyamoto M. 2011. Petrographic and chemical variation among the EH3 chondrites (abstract #1764). 42nd Lunar and Planetary Science Conference. CD-ROM.

Larimer J. W. and Anders E. 1967. Chemical fractionations in meteorites–II. Abundance patterns and their interpretation. *Geochimica et Cosmochimica Acta* 31:1239–1270.

Larimer J. W. and Ganapathy R. 1987. The trace element chemistry of CaS in enstatite chondrites and some implications regarding its origin. *Earth and Planetary Science Letters* 84:123–134.

Larimer J. W. and Wasson J. T. 1988a. Refractory lithophile elements. In *Meteorites and the early solar system*, edited by Kerridge J. F. and Mathews M. S. Tucson, Arizona: University of Arizona Press. pp. 394–415.

Larimer J. W. and Wasson J. T. 1988b. Siderophile element fractionation. In *Meteorites and the early solar system*, edited by Kerridge J. F., and Mathews M. S. Tucson, Arizona: University of Arizona Press. pp. 416–435.

Leitch C. A. and Smith J. V. 1982. Petrography, mineral chemistry and origin of Type I enstatite chondrites. *Geochimica et Cosmochimica Acta* 46:2083–2097.

Lehner S. W. and Buseck P. R. 2009. The highly unequilibrated EH chondrite, Sahara 97072, may be a primitive breccia (abstract #2154). 40th Lunar and Planetary Science Conference. CD-ROM.

Lehner S. W. and Buseck P. R. 2010. TEM study of the sub-micron fraction of matrix in Sahara 97072 (EH3) and ALH 84170 (EH3) (abstract #1880). 41st Lunar and Planetary Science Conference. CD-ROM.

Lehner S. W., Buseck P. R., and McDonough W. F. 2010. Origin of kamacite, schreibersite, and perryite in metal-sulfide nodules of the enstatite chondrite Sahara 97072 (EH3). *Meteoritics & Planetary Science* 45:289–303.

Lehner S. W., Petaev M. I., and Buseck P. R. 2011. Evidence for silicate sulfidation in EH3 metal-sulfide nodules (abstract #9079). In *Workshop on Formation of the First Solids in the Solar System*. Houston, Texas: Lunar and Planetary Institute.

Lehner S. W., Petaev M. I., and Buseck P. R. 2012a. Relation between silicate chondrules and metal-sulfide nodules in EH3 chondrites (abstract #2252). 43rd Lunar and Planetary Science Conference. CD-ROM.

Lehner S. W., Petaev M. I., and Buseck P. R. 2012b. Sulfidation of enstatite in the fine-grained matrix of EH3 Sahara 97072 (abstract #2309). 43rd Lunar and Planetary Science Conference. CD-ROM.

Lehner S. W., Nemeth P., Petaev M. I., and Buseck P. R. 2013a. Origin of nanocrystalline albite in an EH3

sulfidized chondrule (abstract #2500). 44th Lunar & Planetary Science Conference. CD-ROM.
Lehner S. W., Petaev M. I., Zolotov M. Y., and Buseck P. R. 2013b. Formation of niningerite by silicate sulfidation in EH3 enstatite chondrites. *Geochimica et Cosmochimica Acta* 101:34–56.
Lin Y. and El Goresy A. 2002. A comparative study of opaque phases in Qingzhen (EH3) and MacAlpine Hills (EL3): Representatives of EH and EL parent bodies. *Meteoritics & Planetary Science* 37:577–599.
Lodders K. 2003. Solar system abundances and condensation temperatures of the elements. *The Astrophysical Journal* 591:1220–1247.
Piani L., Robert F., Beyssac O., Binet L., Bourot-Denise M., Derenne S., Le Guillou C., Marrocchi Y., Mostefaoui S., Rouzaud J. N., and Thomen A. 2012. Structure, composition, and location of organic matter in the enstatite chondrite Sahara 97096 (EH3). *Meteoritics & Planetary Science* 47:8–29.
Quirico E., Bourot-Denise M., Robin C., Montagnac G., and Beck P. 2011. A reappraisal of the metamorphic history of EH3 and EL3 enstatite chondrites. *Geochimica Et Cosmochimica Acta* 75:3088–3102.
Rubin A. E., Griset C. D., Choi B. G., and Wasson J. T. 2009. Clastic matrix in EH3 chondrites. *Meteoritics & Planetary Science* 44:589–601.
Scott E. R. D. and Krot A. N. 2005. Chondritic meteorites and the high-temperature nebular origins of their components. In *Chondrites and the protoplanetary disk*, edited by Krot A. N., Scott E. R. D., and Reipurth B. San Francisco, California: Astronomical Society of the Pacific. pp. 15–53.
Scott E. R. D., Barber D. J., Alexander C. M. O., and Hutchison R. 1988. Primitive material surviving in chondrites: matrix. In *Meteorites and the early solar system*, edited by Kerridge J. F. and Mathews M. S. Tucson, Arizona: University of Arizona Press. pp. 718–745.
Shukolyukov A. and Lugmair G. W. 2004. Manganese-chromium isotope systematics of enstatite meteorites. *Geochimica et Cosmochimica Acta* 68:2875–2888.
Walker R. J., McDonough W. F., Honesto J., Chabot N. L., McCoy T. J., Ash R. D., and Bellucci J. J. 2008. Modeling fractional crystallization of group IVB iron meteorites. *Geochimica et Cosmochimica Acta* 72:2198–2216.
Wasson J. T. and Kallemeyn G. W. 1988. Compositions of chondrites. *Philosophical Transactions of the Royal Society of London. Series A, Mathematical and Physical Sciences* 325:535–544.
Weisberg M. K. and Prinz M. 1998. Sahara 97096: A highly primitive EH3 chondrite with layered sulfide-metal-rich chondrules (abstract #1741). 29th Lunar and Planetary Science Conference. CD-ROM.
Weisberg M. K., Connolly H. C., Ebel D. S., and Kimura M. 2006. Sulfide-metal nodules in EH3 chondrites (abstract). *Meteoritics & Planetary Science* 41:A186.
Zhang X. V., Benoit P. H., and Sears D. W. G. 1995. The classification and complex thermal history of the enstatite chondrites. *Journal of Geophysical Research-Solid Earth* 100:9417–9438.
Zolensky M., Barrett R., and Browning L. 1993. Mineralogy and composition of matrix and chondrule rims in carbonaceous chondrites. *Geochimica et Cosmochimica Acta* 57:3123–3148.

Table A1. List of elements measured by three methods for bulk Sahara 97072 analysis and those measured using LA-ICPMS. Errors are listed for the analyses of the standards

Method: (ALS CHEMEX)	ME-MS61 Four-acid digestion		ME-MS81 LiB_40_7 fusion ICPMS		ME-ICP06 LiB_40_7 fusion ICP-AES			Mass numbers analyzed with LA-ICPMS[b]
Standard: element	GBM3961c error[a]	MRGeo08 error	G2000 error	SY-4 error	G2000 error	OREAS-13P error	SY-4 error	
Li	0.03	0.09						
Be	0.30	0.10						
Na	0.08	0.05			0.1	0.03	0.04	
Mg	0.06	0.05			0.01	0.01	0.05	^{26}Mg
Al	0.07	0.08			0.05	0.03	0.03	^{27}Al
Si	[c]				0.05	0.01	0.05	^{30}Si
P	0.00	0.01			0.05	0.01	0.01	^{31}P
S	0.07	0.00						^{34}S
K	0.09	0.02			0.03	0.01	0.01	
Ca	0.09	0.02			0.01	0.03	0.04	^{43}Ca
Sc	0.04	0.09						^{45}Sc
Ti	0.09	0.04			0.03	0.09	0.07	^{49}Ti
V	0.06	0.03	0.03	0.1				
Cr	0.07	0.02	0.09	0.2	0.01	0.03	bd	^{53}Cr
Mn	0.08	0.01			0.01	0.03	0.13	^{55}Mn
Fe	0.07	0.02			0.02	0.05	0.03	^{57}Fe
Ni	0.02	0.04	0.01	bd				^{62}Ni
Co	0.00	0.08	0.05	0.17	0.05	0.01	0.07	^{63}Cu
Cu	0.09	0.01	0.04	bd				^{66}Zn

Table A1. *Continued*. List of elements measured by three methods for bulk Sahara 97072 analysis and those measured using LA-ICPMS. Errors are listed for the analyses of the standards

Method: (ALS CHEMEX)	ME-MS61 Four-acid digestion		ME-MS81 LiB_4O_7 fusion ICPMS		ME-ICP06 LiB_4O_7 fusion ICP-AES			Mass numbers analyzed with LA-ICPMS[b]
Standard: element	GBM3961c error[a]	MRGeo08 error	G2000 error	SY-4 error	G2000 error	OREAS-13P error	SY-4 error	
Zn	0.02	0.01	0.05	0.11				
Ga	0.10	0.09	0.07	0.08				^{71}Ga
Ge	0.11	0.00						
As	0.06	0.28						
Se	0.25	0.38						
Rb	0.02	0.07	0.01	0.04				^{85}Rb
Sr	0.03	0.01	0.02	0.05				^{88}Sr
Y	0.02	0.03	0.01	0.05				^{89}Y
Zr	0.00	0.04	0.02	0.08				^{90}Zr
Nb	0.09	0.07	0.09	0.07				^{93}Nb
Mo	0.08	0.04	0.08	bd				^{95}Mo
Pd								^{105}Pd
Ag	0.06	0.11	0.14	bd				
Cd	0.07	0.02						
In	0.09	0.03						
Sn	0.28	0.05	bd	0.01				
Sb	0.05	0.02						
Te	0.03	bd						
Cs	0.08	0.06	0.01	0.05				^{133}Cs
Ba	0.06	0.03	0.02	0.06	0.04	0.15	0.01	^{137}Ba
La	0.10	0.21	0.05	0.06				^{139}La
Ce	0.06	0.20	0.04	0.06				^{140}Ce
Pr			0.03	0.08				
bd			0.04	0.06				146bd
Sm			0.03	0.08				^{147}Sm
Eu			0.02	0.09				^{153}Eu
Gd			0.05	0.08				^{157}Gd
Tb			0.04	0.08				
Dy			0.01	0.07				
Ho			0.01	0.08				^{165}Ho
Er			0.01	0.09				
Tm			0.01	0.09				^{169}Tm
Yb			0.01	0.07				^{172}Yb
Lu			0.02	0.07				^{175}Lu
Hf	0	0	0.01	0.09				
Ta	0.1	0.11	0.11	0.06				
W	0.1	0.2	0.17	bd				^{184}W
Re	0.25	0.22						
Pt								^{195}Pt
Au								^{197}Au
Tl	0.1	0.05	0.1	bd				
Pb	0.05	0.05	0.06	bd				^{208}Pb
Bi	0.08	0.09						
Th	0.1	0.08	0.01	0.06				^{232}Th
U	0.13	0.16	0.03	0.04				^{238}U

[a]Calculated as deviation from the mean of expected range divided by the measured value.
[b]Error and standards for LA-ICPMS are discussed in the Methods section.
[c]Blank spaces represent no measurement for that method.
bd = below detection limit.